

Cite this: *Mater. Adv.*, 2022,  
3, 2104

## Sodium diffusion and dynamics in Na<sub>2</sub>Ti<sub>3</sub>O<sub>7</sub>: neutron scattering and *ab initio* simulations†

Ranjan Mittal,<sup>id</sup>\*<sup>ab</sup> Sajjan Kumar,<sup>ab</sup> Mayanak K. Gupta,<sup>id</sup>\*<sup>ab</sup> Sanjay K. Mishra,<sup>ab</sup>  
Sanghamitra Mukhopadhyay,<sup>id</sup><sup>c</sup> Manh Duc Le,<sup>c</sup> Rakesh Shukla,<sup>d</sup>  
Srungarpu N. Achary,<sup>id</sup><sup>bd</sup> Avesh K. Tyagi,<sup>id</sup><sup>bd</sup> and Samrath L. Chaplot,<sup>id</sup><sup>ab</sup>

We have performed quasielastic and inelastic neutron scattering (QENS and INS) measurements from 300 K to 1173 K to investigate the Na-diffusion and underlying host dynamics in Na<sub>2</sub>Ti<sub>3</sub>O<sub>7</sub>. The QENS and INS measurements were analyzed using *ab initio* molecular dynamics (AIMD) simulations. From these measurements and simulations, we interpreted that at 1173 K, the diffusion of Na is controlled by the localized jumping motion of Na, while at higher temperature (1800 K) AIMD simulations predicted a long range 1-d diffusion of Na through interstitial sites along the crystallographic *a*-axis. Furthermore, calculations using the nudged-elastic-band (NEB) method confirmed the lowest activation energy barrier for Na diffusion along the *a*-axis. In the experimental phonon spectra, the peaks at 10 and 14 meV were dominated by Na dynamics at low temperature, which disappeared on warming, suggesting that low-energy phonons significantly contribute to large Na vibrational amplitude at elevated temperatures that enhance the Na hopping probability. To provide a microscopic understanding of the thermal expansion behaviour and to correlate that with Na dynamics, we have also calculated the mode Grüneisen parameters of the phonons. From this investigation, we have identified that the Na-dominated low-frequency anharmonic phonons strongly contribute to the thermal expansion.

Received 18th October 2021,  
Accepted 6th January 2022

DOI: 10.1039/d1ma00963j

rsc.li/materials-advances

## 1. Introduction

Research on metal ion batteries is progressively helping to make lighter, faster charging, safer, more stable, and more cost-effective batteries.<sup>1,2</sup> Most commercial rechargeable cells are lithium-based and dominate the portable electronics sector due to their high energy density.<sup>3,4</sup> However, the production of these cells may not be profitable in the long run due to the limited resources of lithium. Sodium is one of the most abundant<sup>5</sup> elements (2.8% of elements in the Earth's crust) existing on Earth. Recently Na-based batteries have become popular for the next generation. The energy density of sodium-ion batteries is some 30% lower<sup>6</sup> than that of lithium-ion batteries. However, they can be used for applications where energy density requirements are not as stringent,<sup>7</sup> and may be commercially viable.<sup>8–12</sup> The first sodium–sulfur battery was developed after the discovery of the high-temperature ionic conductor β-alumina, NaAl<sub>11</sub>O<sub>17</sub>.<sup>13</sup> Since then, many Na-ion

conductors have been discovered,<sup>14–17</sup> including the sulfide compounds<sup>18–20</sup> that exhibit very high ionic conductivity suitable for application in batteries. The stability, safety, and performance of these materials are related to their thermodynamic and transport behavior (such as their thermal expansion, phase transitions, electronic and ionic conductivity<sup>21</sup>).

It is important to know the possible mechanism of diffusion and the associated attributes. This information would be helpful to design materials with optimum ionic transport properties. Furthermore, atomic dynamics investigations provide the critical features of diffusion and thermodynamical stability of the material. Hence, it is highly desirable to have an intensive microscopic understanding of the atomic level dynamics.<sup>22,23</sup>

Oxide-based metal-ion conductors have attracted attention<sup>1,2</sup> due to their easy synthesis, low cost, and high stability in variable temperature/pressure ranges. As an important material, Na<sub>2</sub>Ti<sub>3</sub>O<sub>7</sub> has been extensively studied<sup>24–31</sup> for its usage as an anode material. It is known to be a very promising anode compound, especially when it is mixed with carbonaceous materials.<sup>32</sup> Apart from its usage as an anode in sodium batteries, the compound also finds applications in electrochemical devices.<sup>33,34</sup> For example, a study on Na<sub>2</sub>Ti<sub>3</sub>O<sub>7</sub> nanotube/Nafion composite membranes has shown<sup>33</sup> that the addition of Na<sub>2</sub>Ti<sub>3</sub>O<sub>7</sub> nanotubes enhanced the water uptake and reduced the methanol permeability of the composite membranes. The performance, long-term stability, and

<sup>a</sup> Solid State Physics Division, Bhabha Atomic Research Centre, Mumbai, 400085, India. E-mail: rmittal@barc.gov.in, mayankg@barc.gov.in

<sup>b</sup> Homi Bhabha National Institute, Anushaktinagar, Mumbai, 400094, India

<sup>c</sup> ISIS Neutron and Muon Facility, Rutherford Appleton Laboratory, Chilton, Didcot, Oxon OX11 0QX, UK

<sup>d</sup> Chemistry Division, Bhabha Atomic Research Centre, Mumbai, 400085, India

† Electronic supplementary information (ESI) available. See DOI: 10.1039/d1ma00963j



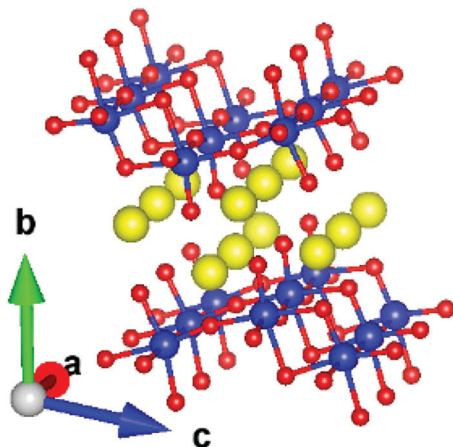


Fig. 1 Crystal structure of  $\text{Na}_2\text{Ti}_3\text{O}_7$ . The color scheme is Ti: blue, Na: yellow and O: red. The lattice parameters of the monoclinic unit cell are:  $a = 3.8008 \text{ \AA}$ ,  $b = 8.5602 \text{ \AA}$ ,  $c = 9.1252 \text{ \AA}$ , and  $\alpha = 101.598^\circ$ .

selectivity of fast potentiometric  $\text{CO}_2$ -sensors consisting of an  $\text{Na}_2\text{Ti}_3\text{O}_7/\text{Na}_2\text{Ti}_6\text{O}_{13}$  electrode have also been studied.<sup>34</sup>  $\text{Na}_2\text{Ti}_3\text{O}_7$  has a layered structure (Fig. 1).<sup>35</sup> The compound has a monoclinic structure<sup>35</sup> with the space group  $P2_1/m$  ( $Z = 2$ ). It has zigzag stepped layers, which are composed of edge-linked distorted  $\text{TiO}_6$  octahedra. The Na ions are intercalated between the layers formed by  $\text{TiO}_6$  octahedra, stacked along the  $b$ -axis. The Na atoms in a layer form channels along the  $a$ -axis.

A study of the ionic conductivity, thermal expansion, and structural properties of  $\text{Na}_2\text{Ti}_3\text{O}_7$  has been reported.<sup>36</sup> The thermodynamic properties of  $\text{Na}_2\text{Ti}_3\text{O}_7$  under high temperature and high pressure have been calculated<sup>37</sup> using DFT with the local density approximation (LDA). However, the LDA calculation is found to significantly underestimate the thermal expansion coefficient in comparison to the experimental data.<sup>36</sup> The zone-centre phonons have also been investigated using Raman scattering and DFT simulations.<sup>38</sup>

The host-flexibility, vacancies, and interstitial sites were proposed to be the critical factors of large-ionic conductivity in recent studies on thiophosphates and Li-argyrodites.<sup>39–42</sup> Our interest is to investigate the possible Na diffusion and influence of host dynamics in  $\text{Na}_2\text{Ti}_3\text{O}_7$  over a broad range of temperatures. Hence, we performed quasielastic and inelastic neutron scattering (QENS and INS) measurements covering dynamics from  $\mu\text{eV}$  to  $\text{meV}$  from  $\sim 300 \text{ K}$  to  $\sim 1173 \text{ K}$ . The QENS technique is mainly suitable for probing the pico-second to nano-second dynamics, typical of superionic solids and liquids. This is a unique technique because it can provide the diffusion hopping timescales and jump lengths, which are essential for the materials design aspect. The jump-length information is helpful to survey the possible pathways for migration, while residence time provides information about the shallowness of the potential energy surface along those pathways. These can be used to tune the material design to optimize the conductivity. The experimental data of the diffusion coefficient<sup>35</sup> of  $\sim 10^{-14} \text{ m}^2 \text{ s}^{-1}$  has been reported for  $\text{Na}_2\text{Ti}_3\text{O}_7$  around the ambient temperature of  $\sim 300 \text{ K}$ . However, this is far too small<sup>43</sup> to be accessible to the atomic scale techniques of AIMD simulations and

QENS, which are good to study the diffusion coefficients of  $\sim 10^{-10} \text{ m}^2 \text{ s}^{-1}$ . The INS data helps to identify the phonon modes which show significant change with temperature. Furthermore, we have performed AIMD and lattice dynamics simulations to supplement these measurements and to have microscopic details of the dynamical process. We have identified the critical influence of the interstitial site on long-range Na diffusion.

## II. Experimental

Monoclinic  $\alpha\text{-Na}_2\text{Ti}_3\text{O}_7$  was prepared by conventional solid-state reaction of  $\text{Na}_2\text{CO}_3$  and rutile-type  $\text{TiO}_2$ .  $\text{TiO}_2$  (rutile,  $\geq 99.9\%$ , Alfa Aesar) was heated at  $1073 \text{ K}$  for  $8 \text{ h}$  and cooled to room temperature before use.  $\text{Na}_2\text{CO}_3$  ( $99\%$ , Sigma-Aldrich) was heated at  $373 \text{ K}$  for  $2 \text{ h}$  and weighed immediately after cooling to room temperature. Appropriate amounts of  $\text{Na}_2\text{CO}_3$  and  $\text{TiO}_2$  in the molar ratio of  $2.01 : 3.00$  for about  $10 \text{ grams}$  of  $\text{Na}_2\text{Ti}_3\text{O}_7$  were mixed thoroughly using acetone as the grinding media. A slight excess ( $0.5 \text{ mole } \%$ ) of  $\text{Na}_2\text{CO}_3$  was required to compensate for the loss of  $\text{Na}_2\text{O}$  at higher temperatures. The homogenous mixture was filled in an alumina crucible and heated at  $773 \text{ K}$  for  $12 \text{ h}$ . The obtained powder was homogenized and pressed into pellets of about  $1\text{-inch}$  diameter and  $1$  to  $1.5 \text{ cm}$  in height. The pellets were heated at  $1073 \text{ K}$  for  $24$ , and then crushed to powder and repelletized. These pellets were again heated at  $1173 \text{ K}$  for  $12 \text{ h}$ . This heating step was repeated three times to obtain single-phase monoclinic  $\alpha\text{-Na}_2\text{Ti}_3\text{O}_7$ . Each time the pellets were crushed and repelletized for the next heating. The white-colored final product was characterized by powder XRD data recorded by using  $\text{Cu K}\alpha$  radiation. Rietveld refinement of the structural model was performed. All the observed peaks and intensities could be accounted for<sup>44</sup> by the monoclinic  $\text{Na}_2\text{Ti}_3\text{O}_7$  (Fig. S1, ESI†<sup>45</sup>). The refined structural details are summarized in Table S1 ESI†<sup>45</sup>, which confirms the good sample quality in terms of phase purity and crystallinity. The  $\text{Na}_2\text{Ti}_3\text{O}_7$  sample is stable in normal atmospheric conditions and does not show sensitivity to air.

As shown in Fig. 1,  $\text{Na}_2\text{Ti}_3\text{O}_7$  has a layered structure. The Na ions are intercalated between the layers formed by  $\text{TiO}_6$  octahedra, stacked along the  $b$ -axis. The diffusion of Na ions is restricted within the intercalated layer, which would lead to a significant broadening in the elastic neutron scattering signal. In QENS techniques, we measure the elastic broadening at different momentum transfer  $Q$  values, which is further used to determine the nature of diffusion. The measurement of QENS spectra has been done using the OSIRIS<sup>46–49</sup> indirect geometry time of flight spectrometer at ISIS. The QENS spectra have been measured at several temperatures from  $300 \text{ K}$  to  $1173 \text{ K}$ . In these experiments, the sample was heated under vacuum in a thin niobium cylindrical cell. We have also measured data from the vanadium standard for the normalization of detector efficiencies and the measurement of the energy resolution of the instrument. The measured data on vanadium with a fixed final energy of  $1.84 \text{ meV}$  with pyrolytic graphite (002) analyzers was fitted to a Gaussian function. The full width at half



maximum (FWHM) of Gaussian was found to be 27  $\mu\text{eV}$ , which is the resolution of OSIRIS. The analysis of data has been performed using the QENS data analysis interface as implemented in Mantid.<sup>50,51</sup> In the case of  $\text{Na}_2\text{Ti}_3\text{O}_7$ , the constituent atoms scatter coherently as well as incoherently (the neutron scattering cross-sections are, Na:  $\sigma_{\text{coh}} = 1.66$  barn,  $\sigma_{\text{incoh}} = 1.62$  barn; Ti:  $\sigma_{\text{coh}} = 1.485$  barn,  $\sigma_{\text{incoh}} = 2.87$  barn; and O:  $\sigma_{\text{coh}} = 4.232$  barn,  $\sigma_{\text{incoh}} = 0.0$  barn). Thus it can be noted that sodium has nearly identical coherent and incoherent cross sections.<sup>52</sup>

The measured neutron scattering intensity is described by the scattering function  $S(Q, E)$ , where  $E$  and  $Q$  are the energy transfer and momentum transfer vector, respectively. The fitting of the QENS measured  $S(Q, E)$  data at various  $Q$  within the dynamic range of the OSIRIS instrument is carried out with one Lorentzian peak and one delta function convoluted with the resolution function of the instrument. The  $Q$ -dependence of the half-width-at-half-maximum (HWHM) of the Lorentzian peak provides<sup>43</sup> direct information about diffusion characteristics.<sup>53,54</sup> For localized diffusion, the HWHM is nearly constant with  $Q$ , while for long-range diffusion, the HWHM in the low  $Q$  regime is characterized by a  $Q^2$  dependence, and the  $Q$ -dependent HWHM data can be analyzed with jump-diffusion models, such as the Chudley–Elliott (C–E)<sup>55</sup> model, and the Hall and Ross (H–R) model.<sup>43,56</sup> None of the above models are applicable in the present case, as there is no long-range diffusion (absence of  $Q^2$  dependence of HWHM at low- $Q$ ); hence, the present case is described by the localized diffusion model. The QENS window used in this experiment on the OSIRIS spectrometer at ISIS is  $-0.5$  to  $0.5$  meV with a pyrolytic graphite (002) analyzer, corresponding to a residence time of  $\sim 10$  ps to 100 ps. The  $Q$ -range of  $0.2$ – $1.8 \text{ \AA}^{-1}$  is usually adequate to capture typical jump lengths of a few  $\text{\AA}$ .

The temperature dependence of the phonon density of states in  $\text{Na}_2\text{Ti}_3\text{O}_7$  was measured<sup>57</sup> using the MARI time of flight direct geometry spectrometer at ISIS, UK. The polycrystalline sample of  $\text{Na}_2\text{Ti}_3\text{O}_7$  was kept in a glass tube of about 10 mm inner diameter. Measurements were carried out at several temperatures from 323 K to 1073 K. The INS measurements were carried out in the energy-loss mode with incident neutron energies of 180 meV and 30 meV. The entire one-phonon spectrum of our sample is accessible by the instrument with the incident energy of 180 meV. The INS measurements with 180 meV and 30 meV have enabled the collection of data in the  $Q$  range from 4 to  $16 \text{ \AA}^{-1}$  and 2 to  $7 \text{ \AA}^{-1}$ , respectively. The two incident energies were used to measure phonon spectra with a reasonable resolution. The data analysis was carried out using Mantid<sup>50,51</sup> software in the incoherent one-phonon approximation. This is a reasonable approximation<sup>57</sup> since the  $Q$ -range of the INS data comprises several Brillouin zones. The INS measured scattering function  $S(Q, E)$  is related<sup>58–60</sup> to the neutron-weighted phonon density of states  $g^{(n)}(E)$  as follows:

$$g^{(n)}(E) = A \left\langle \frac{e^{2W(Q)} E}{Q^2 n(E, T) + \frac{1}{2} \pm \frac{1}{2}} S(Q, E) \right\rangle \quad (1)$$

where the + or – signs correspond to the energy loss or gain of the neutrons, respectively;  $n(E, T) = [\exp(E/k_{\text{B}}T) - 1]^{-1}$ ,  $T$  is

temperature,  $k_{\text{B}}$  is the Boltzmann's constant, and  $A$  is a normalization constant. The quantity between  $\langle \rangle$  represents a suitable average over all  $Q$  values at a given energy.  $2W(Q)$  is the Debye–Waller factor. Usually, the same Debye–Waller factor is assumed for all the atoms, but that assumption is not good if different atoms have very different values of mean-squared displacements. In the present case, the Na atom has a much larger vibrational amplitude than the Ti and O atoms, so we have omitted the Debye–Waller factor in eqn (1) and explicitly retained it in the theoretical calculation of  $g^{(n)}(E)$  as follows:

$$g^{(n)}(E) = B \sum_k \left\{ \frac{\sigma_k}{m_k} \right\} g_k(E) \cdot \exp(-Q^2 \langle u_k^2 \rangle / 3) \quad (2)$$

$B$  is the normalization constant, and  $\sigma_k$ ,  $m_k$ , and  $g_k(E)$  are, respectively, the total neutron scattering cross-section, mass, and partial density of states of the  $k$ th atom in the unit cell.  $2W(Q) = Q^2 \langle u_k^2 \rangle / 3$ , where  $\langle u_k^2 \rangle$  is the mean-squared displacement of the atom  $k$ . The weighting factors  $\frac{\sigma_k}{m_k}$  in the units of barns/amu for O, Na, and Ti atoms are 0.2645, 0.1427, and 0.0909, respectively. The values of neutron scattering lengths for various atoms can be found from ref. 52. As the experimental data analysis assumes a global Debye–Waller factor, this may result in a difference in heights of various peaks in the calculated and experimental phonon spectra.

### III. Computational details

The lattice dynamics and molecular dynamics simulations were performed within the density functional theory framework implemented in the Vienna *Ab initio* Simulation Package (VASP). The calculations are performed using the projector augmented wave (PAW) formalism and with the generalized gradient approximation<sup>61,62</sup> (GGA) exchange–correlation functional parameterization by Perdew, Burke, and Ernzerhof. For lattice dynamics calculations, a  $k$ -point mesh of  $8 \times 4 \times 4$  generated using the Monkhorst–Pack method<sup>63</sup> is used to sample the Brillouin zone. The plane-wave kinetic energy cutoff of 1000 eV is used. The electronic self-consistency convergence criteria for electronic minimization and ionic forces were set to  $10^{-8}$  eV and  $10^{-3}$  eV  $\text{\AA}^{-1}$ , respectively. The phonon calculations were performed using a supercell approach implemented in PHONOPY software.<sup>64</sup> A  $3 \times 2 \times 2$  supercell with 0.01  $\text{\AA}$  displacement was used to derive the force-constant matrix for subsequent phonon calculations.

For *ab initio* molecular dynamics (AIMD) simulation, we used a  $3 \times 2 \times 2$  supercell of the monoclinic unit cell of  $\text{Na}_2\text{Ti}_3\text{O}_7$ . To see the effect of vacancy in the host lattice, we randomly introduced one Na vacancy among 48 Na sites in the  $3 \times 2 \times 2$  supercell. During the diffusion process, the vacancy also migrates to different sites, and hence the choice of the initial vacancy site is not relevant. We used an energy cutoff of 1000 eV. AIMD calculations are computationally expensive,<sup>53,65</sup> hence we have taken only the Gamma  $k$ -point in the Brillouin zone for total energy calculations, and the energy convergence criteria for electronic minimization was  $10^{-6}$  eV. The calculations are performed at 300 K, 1000 K, 1500 K, and 1800 K using an NVT ensemble. The temperature is



controlled using a Nose–Hoover thermostat.<sup>66</sup> The AIMD simulations were performed with a 2 fs step size for  $\sim 60$  ps, where the initial 5 ps data was used for equilibration, and the rest of the trajectory was utilized for the production run. At 1000 K, longer simulations (100 ps) have been done. The mean-squared displacement (MSD,  $\langle u^2 \rangle$ ) of various atoms as a function of time is obtained from the AIMD simulations.<sup>67,68</sup>

We have calculated the thermal expansion behavior in the quasiharmonic approximation.<sup>65</sup> The thermal expansion is the sum of contributions from phonon modes in the entire Brillouin zone.<sup>65,69,70</sup> In the quasiharmonic approximation, the volume thermal expansion coefficient of a crystalline material is given by the following relation:

$$\alpha_V = \frac{1}{BV} \sum_i \Gamma_i C_{vi}(T) \quad (3)$$

The volume dependence of the phonon frequency gives the mode Grüneisen parameter

$$\Gamma_i = -\frac{V}{E_i} \frac{dE_i}{dV} \quad (4)$$

$C_{vi}(T)$  is the specific heat contribution of the  $i$ th phonon mode (of energy  $E_i$ ) at temperature  $T$ , while  $B$  and  $V$  are the bulk modulus and volume of the primitive unit cell, respectively.

## IV. Results and discussion

### A. Na Diffusion, QENS measurements, and AIMD simulations

Fig. 2 shows the measured dynamical neutron scattering function  $S(Q, E)$  of  $\text{Na}_2\text{Ti}_3\text{O}_7$  summed over all the  $Q$  from 300 K to 1173 K, which shows that a significant QENS signal is visible only at 1173 K, indicating the onset of diffusion in the sample. In Fig. 2(c) and Fig. S2 (ESI†<sup>45</sup>), we have shown measured  $S(Q, E)$  at 1173 K. A few Bragg peaks will enter into the window covered by Osiris, complicating the analysis. We have carefully analyzed the raw data and removed the detectors contaminated by Bragg peaks. The  $Q$ -dependence of the HWHM of the fitted Lorentzian peaks at 1173 K is shown in Fig. 2(d). The HWHM does not show much variation with  $Q$ , indicating localized dynamics. Hence, we estimated the time scale of this localized motion by fitting a straight line to HWHM (Fig. 2), and

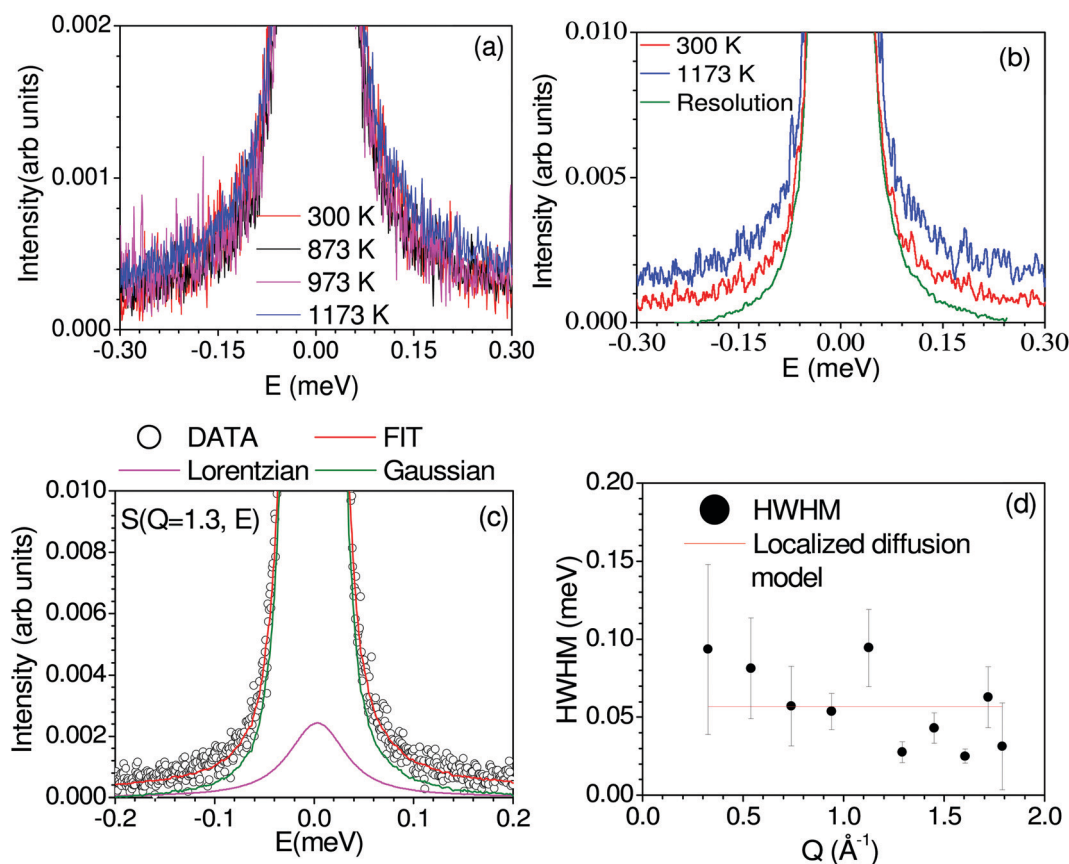


**Fig. 2** (a) Observed dynamical neutron scattering function  $S(Q, E)$  of  $\text{Na}_2\text{Ti}_3\text{O}_7$  integrated over all wave-vector transfers ( $Q$ ) at various temperatures. The experimental  $S(Q, E)$  data at various temperatures have not been normalized to unity at  $E = 0$ . (b) Comparison of the as-observed dynamical neutron scattering function  $S(Q, E)$  of  $\text{Na}_2\text{Ti}_3\text{O}_7$  integrated over all  $Q$  at 300 K and 1173 K and the instrumental resolution (vanadium at 300 K). The data have been normalized to unity at the peak position. (c) Fit of one Lorentzian peak and one delta function convoluted with the resolution function at a selected  $Q = 1.30 \text{ \AA}^{-1}$  slice of  $S(Q, E)$ , and a linear background. (d) The  $Q$  dependent of the variation of the amplitude of half width at half maximum (HWHM) of the Lorentzian peak extracted from the dynamic neutron scattering function  $S(Q, E)$  of  $\text{Na}_2\text{Ti}_3\text{O}_7$  at 1173 K. The fit of the experimental data to the localized diffusion model (red line) model is also shown.





obtained an estimated  $\hbar/\tau \sim 0.06 \pm 0.01$  meV ( $\tau \sim 11 \pm 2$  ps). As the QENS signal is weak, it is difficult to extract the elastic incoherent structure factor (EISF) due to the presence of significant coherent scattering. To supplement the QENS measurement, we performed the  $S(Q, E)$  calculation<sup>43</sup> using AIMD trajectories and estimated the coherent and incoherent contribution of Na dynamics to QENS spectra (Fig. S5, ESI†<sup>45</sup>), and identified that the coherent contribution to QENS is insignificant. As discussed below, the calculated mean-squared amplitude of various atoms shows that other elements do not contribute to QENS. This localized nature of diffusion observed from QENS nicely agrees with the AIMD simulated Na trajectories, which also infers the localized diffusion of Na, as discussed in the next section.

We have performed AIMD simulation to investigate the possible pathways for diffusion and investigate the influence of host dynamics on Na-jumps. The AIMD simulations ( $\sim 50$  ps) in the perfect crystalline phase do not show any signs of diffusion up to 1500 K, indicating the perfect crystalline phase is unlikely or not suitable for Na-diffusion. It is known that vacancies and defects enhance the diffusion behavior.<sup>71–73</sup> The available diffraction data do not identify the very low occupancies of any interstitial sites. So, we have included a typical about 2% Na vacancy in our AIMD simulation that is found useful to initiate the diffusion of Na atoms in our simulations and also help to identify the interstitial sites. We have not considered a higher concentration of vacancies. The interstitial sites get occupied during the diffusion process, as observed in the AIMD

simulations. So, it is not required to introduce Na at the interstitial sites at the start of the AIMD simulations. The calculated MSD of atoms in the structure with one vacancy in the supercell is shown in Fig. 3(a). We have also calculated the anisotropic components of MSD along the Cartesian directions (Fig. S7, ESI†<sup>45</sup>). The component of  $\langle u^2 \rangle$  for Na is largest along the  $a$ -axis ( $x$ -direction), and it shows an increase with time indicating diffusion, while that along the  $b$ -axis ( $y$ -direction) is almost constant with time, indicating no diffusion. From our AIMD simulations on other similar compounds<sup>53</sup> (NaAlSiO<sub>4</sub>), we estimate the statistical errors in MSD of  $\sim 30\%$ . Therefore, we have only used the calculated MSD in Fig. 3 to qualitatively understand the nature of diffusion of Na.

In AIMD simulations of diffusion processes, due to limited computational resources,<sup>74</sup> we are constrained to employ a small simulation cell and perform the simulation for a short duration. Therefore, one often chooses higher temperatures than the experimental temperatures that enhance the diffusion probability. In our sample, the experimental observation of localized diffusion above  $\sim 873$  K is simulated on a 288 atoms cell at above  $\sim 1000$  K. The long-ranged diffusion is simulated at a higher temperature above  $\sim 1500$  K. The experimental observation of localized diffusion up to 1173 K is well supported by our AIMD simulations. By observing the individual squared displacement of Na atoms (Fig. 3(b)) at 1000 K, we observed Na jumps by  $\sim 3.5$  Å. At 1500 K, we find that Na atoms show jumps by  $\sim 3$  to 4 Å and a residence time of  $> 40$  ps (Fig. 3(b)). The residence time reduces at higher temperatures.

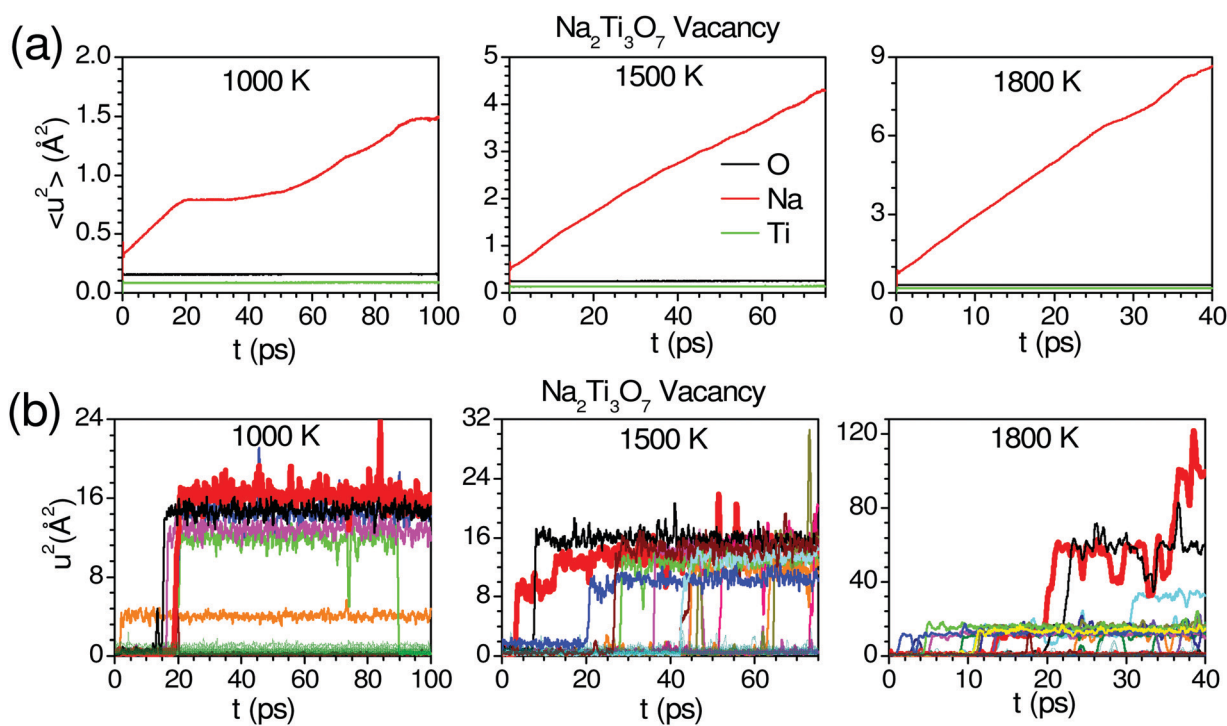


Fig. 3 (a) Time-dependent mean-squared displacements (MSD;  $\langle u^2 \rangle = \langle u_x^2 \rangle + \langle u_y^2 \rangle + \langle u_z^2 \rangle$ ), for various atoms in  $\text{Na}_2\text{Ti}_3\text{O}_7$  with one Na vacancy in a  $(3 \times 2 \times 2)$  supercell. (b) The calculated  $u^2$  of individual Na atoms is represented by different colors. The 3-d trajectories of selected Na atoms (marked by a thick red line) are shown in Fig. 4.



We find that at 1000 K and 1500 K, the Na atom jumps between neighboring sites. However, the jumps are very few in our simulation up to 100 ps. The simulated residence time is larger than  $\sim 11$  ps observed in the QENS experiment at 1173 K. The residence time as found in the AIMD simulations on a small supercell may only be viewed qualitatively, as has also been found in the previous studies.<sup>53</sup> At 1800 K, Na ions show several intra-channel jumps along the *a*-axis, reflecting the long-range diffusion along the *a*-axis. The nature of the jumps is clearly

seen in Fig. 4, which shows the calculated trajectories of selected Na atoms, as well as 2-dimensional projections of the trajectories.

Up to 1500 K, we observe isolated events that involve cooperative jumps of a few atoms to the neighboring regular atomic positions. We note that the probability of cooperative jumps involving simultaneous jumps of several atoms would be rather small compared to independent individual atomic jumps. Indeed, the interstitial sites do get populated at high

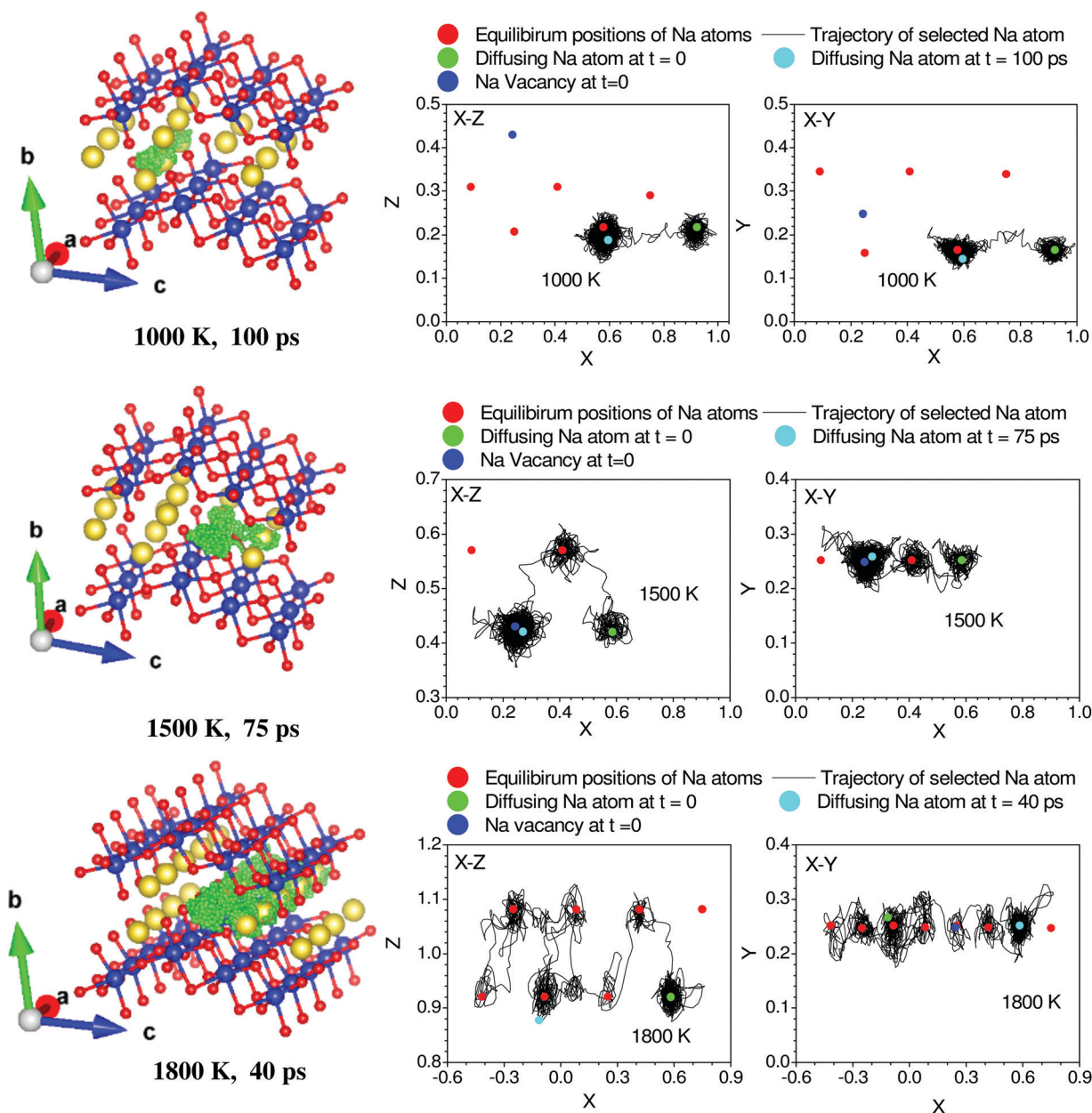


Fig. 4 Trajectory of selected diffusing Na atoms in  $\text{Na}_2\text{Ti}_3\text{O}_7$  at 1000, 1500 and 1800 K. Red, yellow and blue spheres represent O, Na and Ti atoms respectively at their lattice sites. The time-dependent positions of the selected Na atoms are shown by green colored dots. The numbers below each frame indicate the temperature of the simulation and duration of the trajectory of Na. For clarity we have shown a zoomed in version of a part of the  $3 \times 2 \times 2$  supercell to highlight the path of the Na atom. The  $u^2$  of the selected Na atoms in Fig. 3 is shown with thick solid lines. The 2-dimensional projections of the trajectory in the X-Z and X-Y planes are also shown for each of the trajectories. The fractional co-ordinates (*x*, *y*, *z*) are shown with respect to the  $3 \times 2 \times 2$  supercell.



temperatures that enable diffusion. Individual jumps are not feasible in the absence of regular vacant positions or low-energy interstitial positions. At higher temperatures, when sufficient kinetic energy is available, it may be possible to observe individual jumps, where the jumping atoms halt (Fig. 4) for a short while at interstitial positions. Indeed, at 1800 K, this interstitial occupancy is observed, and atoms are found to undergo several jumps, leading to long-range diffusion. We note that the jumping atoms halt (Fig. 4) for a short while at the interstitial position, and the halting time, as well as the total jump time, are much smaller than the residence time. Therefore, this may be considered as a single jump. The calculated Na occupation probability density iso-surface plot at 1500 K (Fig. 5) does not show significant probability at the interstitial sites, while at 1800 K, there are jumps at the interstitial positions, enabling the long-range diffusion.

The nudged elastic band (NEB) method is used to determine the activation energy barrier between two energy minima.<sup>75</sup> In the perfect crystalline case, we estimated the energy barrier by moving two Na atoms simultaneously, as shown in Fig. 6, finding an energy barrier of 1.0 eV. We have also computed the activation barrier for the vacancy structure. The barrier energy profile for intra-channel and inter-channel jumps are 0.27 eV and 0.5 eV, respectively (Fig. 6). Interestingly, we observe a much smaller barrier for intra-channel diffusion than inter-channel diffusion. An energy barrier  $\sim 0.34$  eV is estimated from conductivity measurements (297 K to 324 K),<sup>35</sup> which shows a fair agreement with our calculated barrier energy in Na-vacancy. It is also important to mention that the conductivity measurements give effective barrier energy from both intra- and inter-channel jump processes. To further investigate the differences in intra- and inter-channel, we have analyzed the intermediate NEB images. We found that the inter-channel Na hopping involves the rotation of neighboring Ti–O bonds by  $\sim 3^\circ$ – $7^\circ$ , which results in an angular distortion of the neighboring TiO<sub>6</sub> octahedron, while an intra-channel jump has the least effect on neighboring TiO<sub>6</sub>. We note that a relatively firm 2-d layered structure costs significantly to rotate the TiO<sub>6</sub> units and, in turn, leads to a larger barrier energy.

We have used the GGA-PBE functional for NEB calculation; the estimated barrier energy for Na migrations qualitatively explains the easy direction of migrations. Although a more accurate calculation of barrier energy based on a hybrid functional and with a different basis set may provide better estimates,<sup>76,77</sup> the qualitative understanding of the physics of diffusion behaviour would not change. It is also important to note that hybrid calculations are very expensive, in particular with a relatively larger number of atoms.

The barrier energy for the vacancy structure between two nearest Na-sites along the *a*-axis has also been calculated from the free-energy landscape of the Na ion ( $F_{\text{Na}}(r)$ ) at 1800 K using the following relation:<sup>78</sup>

$$F_{\text{Na}}(r) = -k_{\text{B}}T \ln(P_{\text{Na}}(r))$$

Here  $k_{\text{B}}$ ,  $T$ , and  $P_{\text{Na}}(r)$  are the Boltzmann constant, temperature, and probability of Na occupancy at a distance  $r$  from the

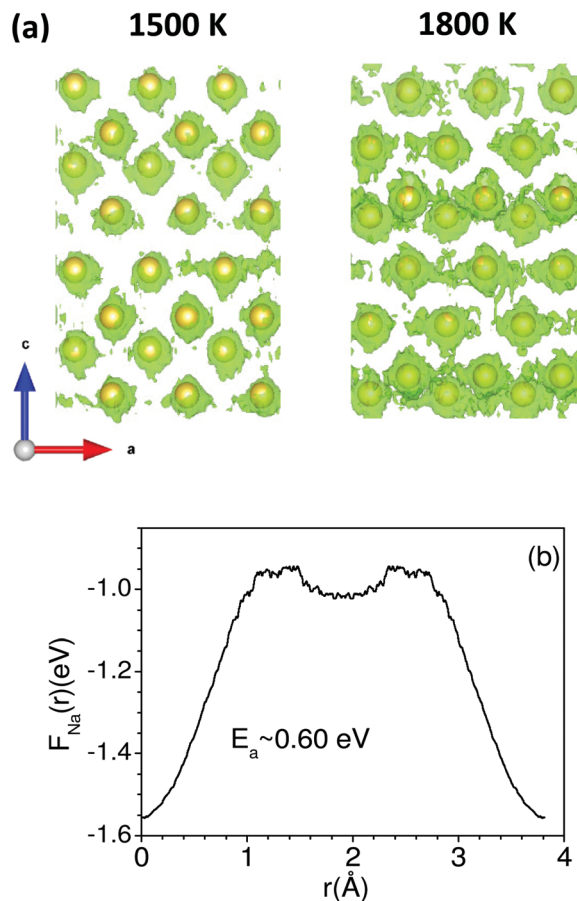


Fig. 5 (a) The calculated Na iso-surface probability (green dots) in the vacancy structure of Na<sub>2</sub>Ti<sub>3</sub>O<sub>7</sub> at 1500 K and 1800 K. Yellow spheres show equilibrium Na sites. Both the panels are shown in the *a*–*c* plane, where the *c*-axis is vertical and the *a*-axis is horizontal. (b) The calculated free energy ( $F_{\text{Na}}(r)$ ) at 1800 K from the Na probability distribution between two nearest Na-sites along the *a*-axis. ' $r$ ' is the distance from the Na sites along the *a*-axis.

equilibrium Na position. The calculated  $F_{\text{Na}}(r)$  is shown in Fig. 5(b), which indicates the barrier of  $E_{\text{a}} \sim 0.60$  eV for Na migration. On the other hand, the nudged elastic band (NEB) method gives (Fig. 6(a)) a value of 0.27 eV for the intra-channel diffusion. It may be noted that in the NEB method, we simulated a single Na jump from a regular site to a vacant site, while  $F_{\text{Na}}(r)$  is estimated from the AIMD trajectory and includes all possible events such as single and correlated jumps; hence it may give a more realistic estimate of  $E_{\text{a}}$ . The energy barrier calculations from both methods show a local minimum in the barrier energy profiles at half of the distance ( $\sim 1.9$  Å) between two Na atoms, indicating interstitial positions along the *a*-axis that may enable the long-range diffusion.

Soft bond valence sum analysis<sup>79</sup> based on structure data has been successfully used to explore the diffusion pathways in many systems as an initial guess and may sometimes accurately predict pathways.<sup>80,81</sup> In order to search for other possibilities and supplement the AIMD predictions, we have performed soft bond valence sum analysis using the structural data from





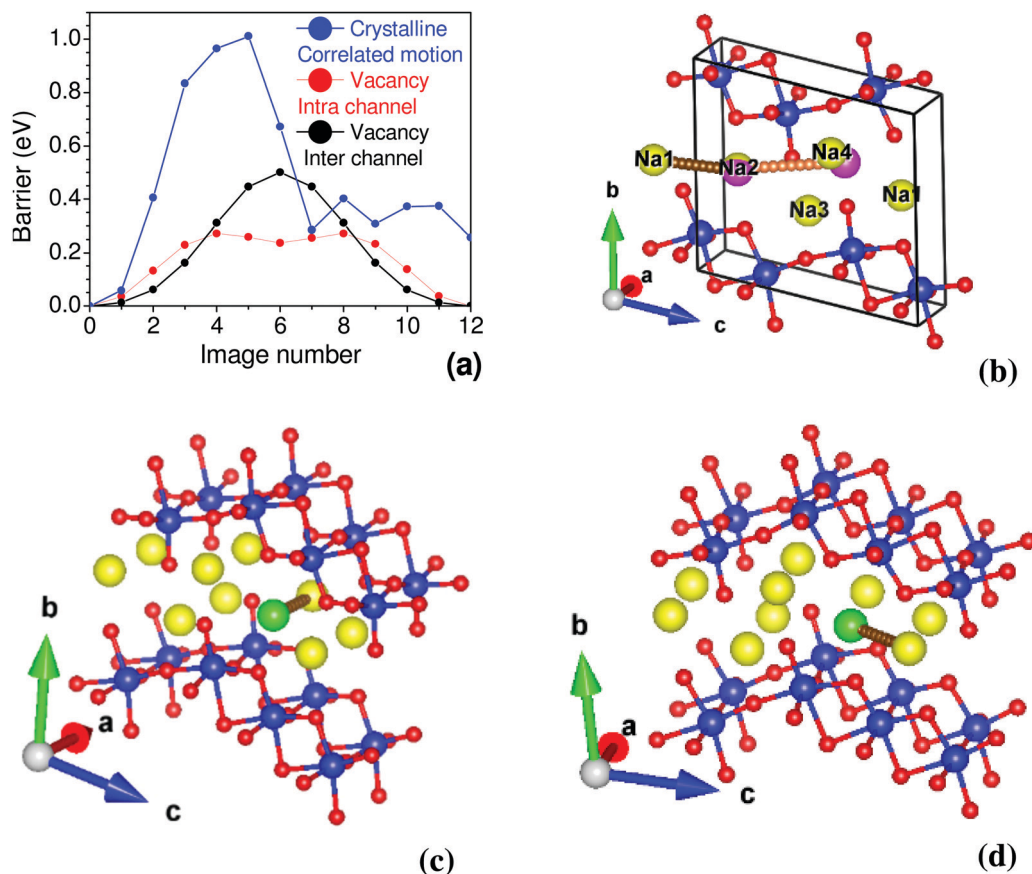


**Fig. 6** (a) The estimated activation energy barrier from the nudged elastic band (NEB) method. (b) The path of the Na atom for estimation of the energy barrier in perfect crystalline structure. The correlated motion of Na1 and Na2 are shown by brown and orange circles. Na1 moves to the position of Na2, while Na2 moves to an interstitial position. (c) and (d) are the paths of the Na atom for estimation of the energy barrier in the vacancy structure, for Na movement in the intra-channel and inter-channel cases, respectively. In (c) and (d) we have shown a zoomed in version of a part of the  $3 \times 2 \times 2$  supercell to highlight the path of Na atom for estimation of the energy barrier. The color scheme is Ti: blue and O: red. Na at regular sites is shown by a yellow color. The green color in (c) and (d) is the Na vacancy, and the Na-path connects the green circle with a yellow circle. Small brown and orange circles are the position of Na atoms in various images of NEB simulation. The magenta circle in (b) is the position of the Na2 atom at the interstitial site.

ref. 35. The contribution of individual Na sites to the Na-ion conduction has been estimated by performing bond valence energy landscape (BVEL) map analysis implemented in FULL-PROF software<sup>82</sup> (Fig. 7). For the BVEL map, we have chosen an iso-energy surface of 0.34 eV, which corresponds to an experimentally estimated barrier energy<sup>35</sup> from conductivity measurements. We have also taken a different cutoff level of 0.2 eV (Fig. 7). We find that for the lower 0.2 eV cutoff, the Na atoms are mobile along the *a*-axis, while for the higher 0.34 eV cutoff (Fig. 7) the Na ions are mobile in the *a*-*c* plane. As noted above, due to the layered structure of the material, the conductivity along the *b*-axis is fully suppressed. Furthermore, BVEL analysis did not predict any other new pathways for Na diffusion, which confirms that our AIMD simulations ( $\sim 50$  ps) have taken care of all possible pathways.

### B. INS measurements and lattice dynamics

The measured temperature dependence of the phonon spectra of  $\text{Na}_2\text{Ti}_3\text{O}_7$  from 323 K to 1023 K are shown in Fig. 8. The

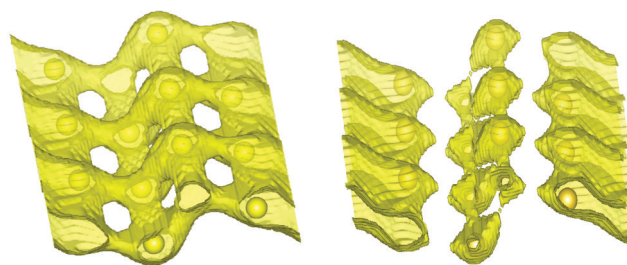


**Fig. 7** The bond valence energy landscape (BVEL) map of  $\text{Na}_2\text{Ti}_3\text{O}_7$  as estimated from the structural data<sup>35</sup> at 300 K. Left and right figures correspond to the iso-energy surface of 0.34 eV and 0.20 eV, respectively. The yellow spheres show the equilibrium positions of Na. The map is shown in the *a*-*c* plane, where the *a*-axis is along the one-dimensional channel formed by Na atoms.

measurements performed with an incident energy of 180 meV provide an energy resolution of  $\sim 7$  meV, and enable the collection of data in the entire spectral range. The large





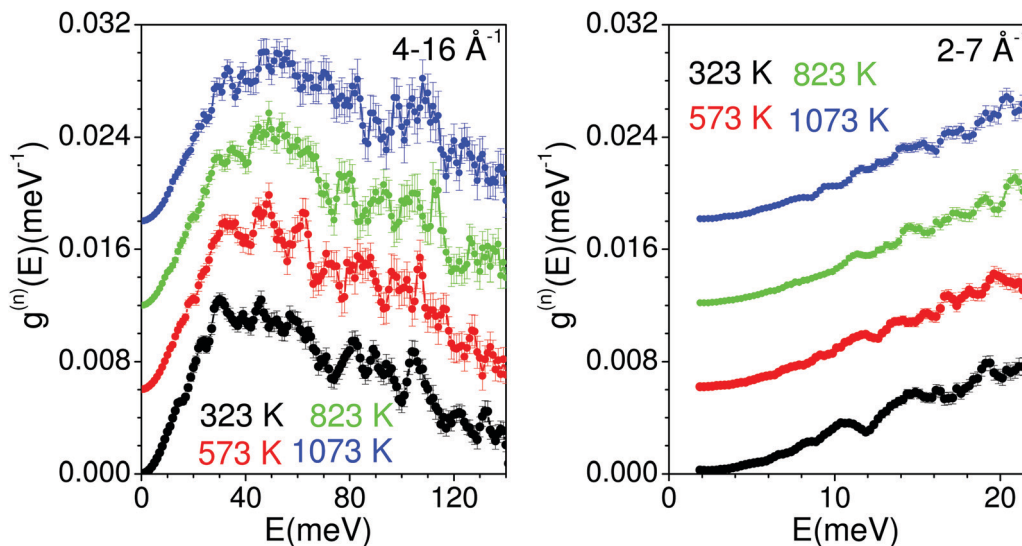


Fig. 8 The experimentally measured neutron-weighted phonon density of states in  $\text{Na}_2\text{Ti}_3\text{O}_7$  at various temperatures. The multi-phonon contribution has been corrected using a standard procedure at ISIS.

incident energy has enabled the collection of data at a high momentum transfer vector  $Q$  range from 4 to  $16 \text{ \AA}^{-1}$ . However, the data collection at such large  $Q$  values would be contaminated from a large multi-phonon contribution, which has been corrected using the standard formalism as discussed in ref. 83. The data collection at large  $Q$  values (from  $\sim 4$  to  $16 \text{ \AA}^{-1}$ ) would be contaminated from large multi-phonon contribution, which has been corrected using the standard formalism. However, it is very difficult to treat the multi-phonon contribution precisely in the experimental data due to the use of a global Debye–Waller factor. This usually leads to some intensity beyond the actual range of density of states (DOS) in measurements.

The phonon spectra measured with an incident energy of 180 meV show sharp peaks at 30 meV, 38 meV, 46 meV, 50 meV, 60 meV, 80 meV, 90 meV and 107 meV. The peak structure is gradually broadened on warming, and peaks in the DOS start merging at 823 K. To identify the individual atomic contribution in the INS spectra, we calculated the atomic-species resolved neutron-weighted DOS and compared it with the 323 K measurement (Fig. 9(a)). The calculation shows (Fig. 9(a)) that the measured neutron-weighted DOS is dominated by O-atom dynamics. Fig. 9(c) shows the total and partial density of states. The low energy spectra below 20 meV have a significant contribution from Na dynamics. Ti has a low- to mid-energy range contribution. The calculated range of phonon spectra matches very well with our experimental data and Raman measurements.<sup>38</sup> It is interesting to note that the Na dominant contribution at low energy reflects the softer bonding of Na to the host. However, the significant overlap of Na–DOS with O- and Ti–DOS also indicates that the Na dynamics is affected by the dynamics of the host elements.

The INS spectra have also been measured with an incident neutron energy of 30 meV to probe the low energy phonons with a better energy resolution of  $\sim 1$  meV. The measurements

enabled the collection of neutron spectra up to 22 meV in the  $Q$  range from 2 to  $7 \text{ \AA}^{-1}$ . The low energy spectra show that the peaks at 10, 14 and 19 meV are predominantly due to Na atoms, which get weakened and broadened with the increase in temperature (Fig. 8 and 9(b), (c)). The calculated neutron-weighted phonon density of states at 300 and 1100 K is shown in Fig. 9(b). The Na contribution in Fig. 9 is not very prominent. But still we notice that the peaks at  $\sim 10$  meV and 14 meV are largely contributed from Na dynamics at 300 K, which significantly reduce at 1100 K due to the increase in the Debye–Waller factor. Thus, the disappearance of the 10 and 14 meV peaks on warming (Fig. 7) is attributed to the large vibrational amplitude of Na at high temperatures. The increase in the vibrational amplitude of the Na atoms at high temperatures may enhance the Na hopping probability. Hence, these low-energy Na modes could play an important role in Na diffusion.

### C. Calculated and experimental thermal expansion behavior

We have calculated the pressure dependence of the phonon spectrum of  $\text{Na}_2\text{Ti}_3\text{O}_7$  and obtained the mode Grüneisen parameters in the entire Brillouin zone. The calculated mode Grüneisen parameter  $\Gamma$  of phonons of energy  $E$ , averaged over the entire Brillouin zone, as a function of phonon energy ( $E$ ) is shown in Fig. 10(a). It can be seen that the low-energy phonon modes below 20 meV have very large positive values of  $\Gamma$  up to +10. The calculated volume thermal expansion coefficient ( $\alpha_v$ ) is shown in the inset of Fig. 10(a). Our calculations are found to be in excellent agreement (Fig. 10(b)) with the available experimental data from the literature.<sup>36</sup> Previously,  $\alpha_v$  for  $\text{Na}_2\text{Ti}_3\text{O}_7$  has been calculated<sup>37</sup> within the local density approximation (LDA) and found to be  $\sim 21 \times 10^{-6} \text{ K}^{-1}$  at 1000 K, which is significantly underestimated as compared to our calculations of  $44 \times 10^{-6} \text{ K}^{-1}$  at 1000 K within the



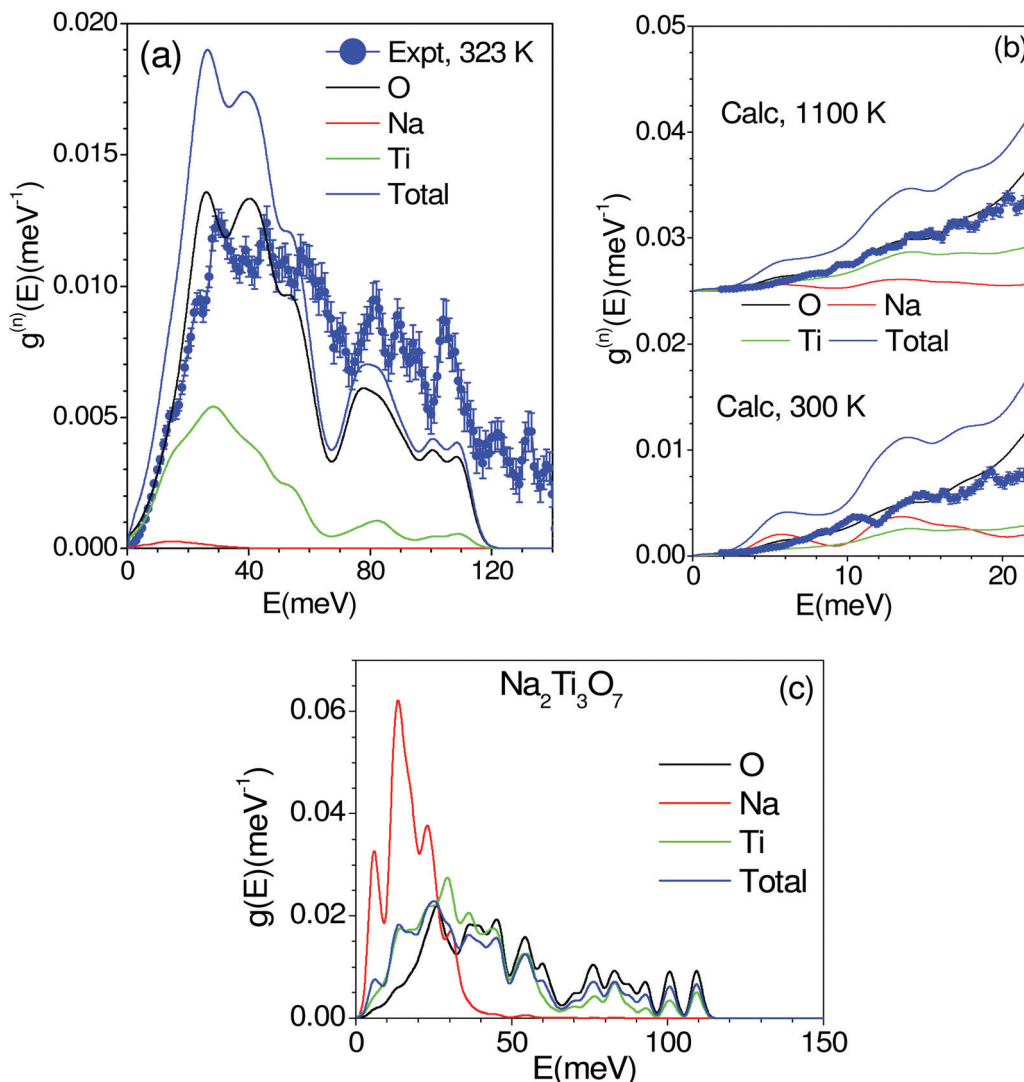


**Fig. 9** (a) The calculated (0 K) and experimental (323 K) neutron-weighted phonon density of states in  $\text{Na}_2\text{Ti}_3\text{O}_7$ . The phonon spectra have been calculated from *ab initio* lattice dynamics. The calculated neutron-weighted partial contributions from various atoms are also shown. The average  $Q$  value of  $Q = 10 \text{ \AA}^{-1}$  has been taken for the Debye–Waller factor. The calculated spectra have been broadened with the a Gaussian of full width at half maximum of 4% of the incident energy of 180 meV, which correspond to the resolution of the experiment. (b) The calculated neutron-weighted phonon density of states of  $\text{Na}_2\text{Ti}_3\text{O}_7$  including the effect of the Debye–Waller factor. The calculated neutron-weighted partial contributions from various atoms are also shown. The calculated spectra have been broadened with the Gaussian of full width of half maximum of 1 meV. The average  $Q$  value of  $Q = 5 \text{ \AA}^{-1}$  has been taken for the Debye–Waller factor. The experimental data (blue circles with solid line) at 323 K and 1073 K are also shown for comparison with the calculations at 300 K and 1100 K respectively. (c) The calculated total and the partial phonon densities of states of various atoms in  $\text{Na}_2\text{Ti}_3\text{O}_7$  from *ab initio* lattice dynamics.

generalized gradient approximation (GGA) as well as the experimental value (inset of Fig. 10(a)).

Furthermore, we have calculated the contribution (Fig. 10(c)) to the volume thermal expansion coefficient from phonons of energy  $E$ , averaged over the entire Brillouin zone, as a function of phonon energy ( $E$ ) at 300 K. We find that the phonon modes of up to 40 meV contribute the most to  $\alpha_v$ . The contribution of phonons of energy  $E$  to the mean-squared amplitude ( $u^2$ ) of various atoms at 300 K shows (Fig. 10(d)) that Na has very large values for phonons of an energy below 20 meV, while contributions from Ti and O are very small. The structure of  $\text{Na}_2\text{Ti}_3\text{O}_7$  consists of layers of distorted  $\text{TiO}_6$  octahedra, with Na ions

intercalated in between the layers. The large value of  $u^2$  for phonon modes below 20 meV indicates that the large displacement of Na within a layer is mainly responsible for the large values of  $\alpha_v$  for  $\text{Na}_2\text{Ti}_3\text{O}_7$ .

## V. Conclusions

We have observed significant broadening in the QENS spectra in  $\text{Na}_2\text{Ti}_3\text{O}_7$  at 1173 K, and interpreted the same using AIMD simulations. The AIMD simulations show the diffusion of Na to be preferentially one-dimensional through channels along the



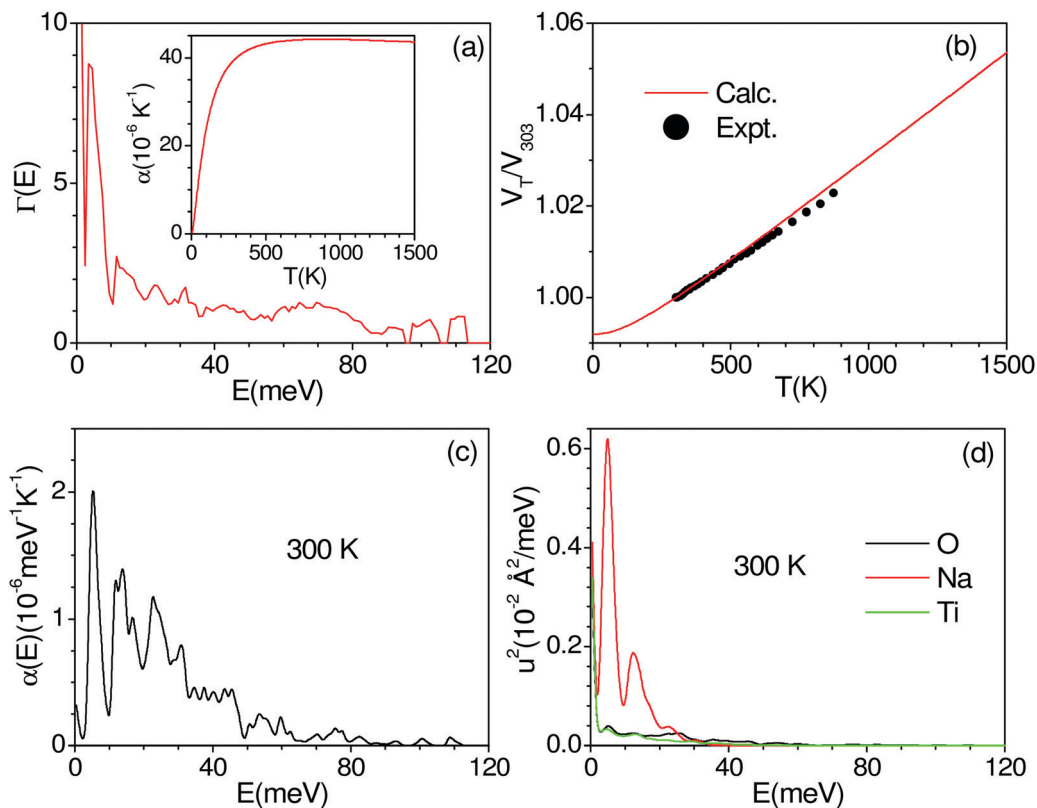


**Fig. 10** (a) The calculated mode Grüneisen parameter  $\Gamma$  of phonons of energy  $E$ , averaged over the entire Brillouin zone, as a function of phonon energy ( $E$ ). The inset in (a) shows the calculated volume thermal expansion coefficients  $\alpha_V$ . (b) The calculated and experimental (closed symbols)<sup>36</sup> volume thermal expansion in  $\text{Na}_2\text{Ti}_3\text{O}_7$ . The contribution of phonon modes of energy  $E$ , averaged over the entire Brillouin zone, (c) to volume thermal expansion coefficients at 300 K, and (d) to the mean-squared amplitude of various atoms in  $\text{Na}_2\text{Ti}_3\text{O}_7$  at 300 K.

crystallographic  $a$ -axis. The calculated activation energy barrier for the intra-channel diffusion (along the  $a$ -axis) is found to be much smaller in comparison to that for the inter-channel diffusion, which is consistent with the AIMD simulations. Furthermore, we have reported INS measurements of the phonon DOS and lattice dynamics calculations. The Na phonon modes at low energies below 20 meV are found to weaken significantly in intensity at high temperatures due to the large Na vibrational amplitudes. The volume thermal expansion coefficient has also been calculated using the quasiharmonic approximation. The low-energy Na phonon modes are found to lead to a high value of the volume thermal expansion coefficient in  $\text{Na}_2\text{Ti}_3\text{O}_7$ .

## Author contributions

R. M., M. K. G. and S. L. C. formulated the problem and planned the experiments and *ab initio* calculations. R. M., S. L. C., S. M. and M. D. L. performed the Neutron Scattering experiments. RM, M. K. G. and S. K. performed AIMD simulations. S. K., S. K. M., M. K. G., R. M., S. M., S. L. C. and M. D. L. analysed the experimental and simulated data. R. A., S. N. A., and A. K. T. synthesized and characterized the samples. M. K. G., R. M., S. L. C. and S. K. M. wrote the manuscript, and all authors commented on it.

## Conflicts of interest

The authors declare no conflict of interest.

## Acknowledgements

The use of the ANUPAM super-computing facility at BARC is acknowledged. The authors thank the Department of Science and Technology, India (SR/NM/Z-07/2015) for the financial support and Jawaharlal Nehru Centre for Advanced Scientific Research (JNCASR) for managing the project. The authors also thank STFC, UK, for the beam-time at ISIS and also availing the travel support from the Newton fund, ISIS, UK. Experiments at the ISIS Neutron and Muon Source were supported by a beamtime allocation RB1868015 and RB1910264 from the Science and Technology Facilities Council. SLC thanks the Indian National Science Academy for the financial support of the INSA Senior Scientist position.

## References

- 1 J. W. Choi and D. Aurbach, *Nat. Rev. Mater.*, 2016, **1**, 16013.
- 2 Y. Kato, S. Hori, T. Saito, K. Suzuki, M. Hirayama, A. Mitsui, M. Yonemura, H. Iba and R. Kanno, *Nat. Energy*, 2016, **1**, 16030.





- 3 M. Wakihara, *Mater. Sci. Eng., R*, 2001, **33**, 109–134.
- 4 J. B. Goodenough, *Energy Storage Mater.*, 2015, **1**, 158–161.
- 5 W. Song, X. Ji, C. Pan, Y. Zhu, Q. Chen and C. E. Banks, *Phys. Chem. Chem. Phys.*, 2013, **15**, 14357–14363.
- 6 J.-M. Tarascon, *Joule*, 2020, **4**, 1616–1620.
- 7 B. L. Ellis and L. F. Nazar, *Curr. Opin. Solid State Mater. Sci.*, 2012, **16**, 168–177.
- 8 Y.-E. Zhu, X. Qi, X. Chen, X. Zhou, X. Zhang, J. Wei, Y. Hu and Z. Zhou, *J. Mater. Chem. A*, 2016, **4**, 11103–11109.
- 9 X. Li, S. Guo, F. Qiu, L. Wang, M. Ishida and H. Zhou, *J. Mater. Chem. A*, 2019, **7**, 4395–4399.
- 10 J. Alvarado, G. Barim, C. D. Quilty, E. Yi, K. J. Takeuchi, E. S. Takeuchi, A. C. Marschilok and M. M. Doeff, *J. Mater. Chem. A*, 2020, **8**, 19917–19926.
- 11 G. Yan, S. Mariyappan, G. Rousse, Q. Jacquet, M. Deschamps, R. David, B. Mirvaux, J. W. Freeland and J.-M. Tarascon, *Nat. Commun.*, 2019, **10**, 1–12.
- 12 J. Wang, Y. Wang, D. H. Seo, T. Shi, S. Chen, Y. Tian, H. Kim and G. Ceder, *Adv. Energy Mater.*, 2020, **10**, 1903968.
- 13 F. Yung, Y. Yao and J. T. Kummer, *J. Inorg. Nucl. Chem.*, 1967, **29**, 2453–2475.
- 14 S.-H. Bo, Y. Wang and G. Ceder, *J. Mater. Chem. A*, 2016, **4**, 9044–9053.
- 15 C. Yu, S. Ganapathy, N. J. J. de Klerk, E. R. H. van Eck and M. Wagemaker, *J. Mater. Chem. A*, 2016, **4**, 15095–15105.
- 16 S. Muy, J. C. Bachman, L. Giordano, H.-H. Chang, D. L. Abernathy, D. Bansal, O. Delaire, S. Hori, R. Kanno, F. Maglia, S. Lupart, P. Lamp and Y. Shao-Horn, *Energy Environ. Sci.*, 2018, **11**, 850–859.
- 17 T. Krauskopf, S. Muy, S. P. Culver, S. Ohno, O. Delaire, Y. Shao-Horn and W. G. Zeier, *J. Am. Chem. Soc.*, 2018, **140**, 14464–14473.
- 18 A. Hayashi, K. Noi, A. Sakuda and M. Tatsumisago, *Nat. Commun.*, 2012, **3**, 856.
- 19 K. Noi, A. Hayashi and M. Tatsumisago, *J. Power Sources*, 2014, **269**, 260–265.
- 20 M. Guin and F. Tietz, *J. Power Sources*, 2015, **273**, 1056–1064.
- 21 P. H. Jampani, O. Velikokhatnyi, K. Kadakia, D. H. Hong, S. S. Damle, J. A. Poston, A. Manivannan and P. N. Kumta, *J. Mater. Chem. A*, 2015, **3**, 8413–8432.
- 22 Y. Wang, W. D. Richards, S. P. Ong, L. J. Miara, J. C. Kim, Y. Mo and G. Ceder, *Nat. Mater.*, 2015, **14**, 1026.
- 23 Q. Wang, J. A. Jackson, Q. Ge, J. B. Hopkins, C. M. Spadaccini and N. X. Fang, *Phys. Rev. Lett.*, 2016, **117**, 175901.
- 24 L. Luo, Y. Zhen, Y. Lu, K. Zhou, J. Huang, Z. Huang, S. Mathur and Z. Hong, *Nanoscale*, 2020, **12**, 230–238.
- 25 P. Senguttuvan, G. Rousse, V. Seznec, J.-M. Tarascon and M. R. Palacin, *Chem. Mater.*, 2011, **23**, 4109–4111.
- 26 Y. Cao, Q. Ye, F. Wang, X. Fan, L. Hu, F. Wang, T. Zhai and H. Li, *Adv. Funct. Mater.*, 2020, 2003733.
- 27 T. K. Saothayanun, T. T. Sirinakorn and M. Ogawa, *Inorg. Chem.*, 2020, **59**, 4024–4029.
- 28 M. A. Tsiamtsouri, P. K. Allan, A. J. Pell, J. M. Stratford, G. Kim, R. N. Kerber, P. C. Magusin, D. A. Jefferson and C. P. Grey, *Chem. Mater.*, 2018, **30**, 1505–1516.
- 29 M. Mori, Y. Kumagai, K. Matsunaga and I. Tanaka, *Phys. Rev. B: Condens. Matter Mater. Phys.*, 2009, **79**, 144117.
- 30 L. Zhang, L. Chen, X. Fan, X. Xiao, J. Zheng and X. Huang, *J. Mater. Chem. A*, 2017, **5**, 6178–6185.
- 31 C. Wu, W. Hua, Z. Zhang, B. Zhong, Z. Yang, G. Feng, W. Xiang, Z. Wu and X. Guo, *Adv. Sci.*, 2018, **5**, 1800519.
- 32 Z. Zhou, H. Xiao, F. Zhang, X. Zhang and Y. Tang, *Electrochim. Acta*, 2016, **211**, 430–436.
- 33 Y. Wei, L. Shen, Z. Wang, W.-D. Yang, H. Zhu and H. Liu, *Int. J. Hydrogen Energy*, 2011, **36**, 5088–5095.
- 34 M. Holzinger, J. Maier and W. Sitte, *Solid State Ionics*, 1996, **86**, 1055–1062.
- 35 Y. Fukuzumi, W. Kobayashi and Y. Moritomo, *J. Adv. Nanomater.*, 2016, **1**, 39.
- 36 M. Dynarowska, J. Kotwiński, M. Leszczynska, M. Marzantowicz and F. Krok, *Solid State Ionics*, 2017, **301**, 35–42.
- 37 H. Zhang and H. Wu, *Phys. Status Solidi A*, 2008, **245**, 37–43.
- 38 F. L. R. Silva, *J. Raman Spectrosc.*, 2018, **49**, 538–548.
- 39 L. Zhou, A. Assoud, Q. Zhang, X. Wu and L. F. Nazar, *J. Am. Chem. Soc.*, 2019, **141**, 19002–19013.
- 40 B. J. Morgan, *Chem. Mater.*, 2021, **33**, 2004–2018.
- 41 R. Schlenker, A.-L. Hansen, A. Senyshyn, T. Zinkevich, M. Knapp, T. Hupfer, H. Ehrenberg and S. Indris, *Chem. Mater.*, 2020, **32**, 8420–8430.
- 42 Z. Zhu, I.-H. Chu, Z. Deng and S. P. Ong, *Chem. Mater.*, 2015, **27**, 8318–8325.
- 43 M. Bee, *Quasi Elastic Neutron Scattering*, Adam Hilger, IOP Publishing Ltd, Bristol, England, 1988.
- 44 O. Yakubovich and V. Kireev, *Crystallogr. Rep.*, 2003, **48**, 24–28.
- 45 See Supplementary Material for details about characterization and experimental QENS spectra for Na<sub>2</sub>Ti<sub>3</sub>O<sub>7</sub> at 1173 K. It also contains results from AIMD simulations and analysis of QENS spectra.
- 46 R. Mittal and *et al.*, *Na-Dynamics in Solid Ionic Conductors: 11Al<sub>2</sub>O<sub>3</sub>-Na<sub>2</sub>O and Na<sub>2</sub>Ti<sub>3</sub>O<sub>7</sub>*, STFC ISIS Neutron and Muon Source, DOI: 10.5286/ISIS.E.RB1910264.
- 47 F. Demmel, D. McPhail, J. Crawford, K. Pokhilchuk, V. G. Sakai, S. Mukhopadhyay, M. T. F. Telling, F. J. Bermejo, N. T. Skippe and F. Fernandez-Alonso, *Eur. Phys. J. Web Conf.*, 2015, **83**, 03003.
- 48 M. T. Telling, S. I. Campbell, D. Engberg, D. M. y. Marero and K. H. Andersen, *Phys. Chem. Chem. Phys.*, 2016, **18**, 8243.
- 49 B. L. Vidal, E. Oram, R. A. Baños, L. C. Pardo, S. Mukhopadhyay and F. Fernandez-Alonso, *J. Phys.: Conf. Ser.*, 2018, **1021**, 012012.
- 50 S. Mukhopadhyay, B. Hewer, S. Howells and A. Markvardsen, *Physica B: Condensed Matter*, 2019, **563**, 41–49.
- 51 O. Arnold, J.-C. Bilheux, J. Borreguero, A. Buts, S. I. Campbell, L. Chapon, M. Doucet, N. Draper, R. F. Leal and M. Gigg, *Nucl. Instrum. Methods Phys. Res., Sect. A*, 2014, **764**, 156–166.
- 52 V. F. Sears, *Neutron News*, 1992, **3**, 26–37.
- 53 M. K. Gupta, R. Mittal, S. Kumar, B. Singh, N. H. Jalarvo, O. Delaire, R. Shukla, S. N. Achary, A. I. Kolesnikov,



- A. K. Tyagi and S. L. Chaplot, *J. Mater. Chem. A*, 2021, **9**, 16129–16136.
- 54 T. Willis, D. Porter, D. Voneshen, S. Uthayakumar, F. Demmel, M. Gutmann, M. Roger, K. Refson and J. Goff, *Sci. Rep.*, 2018, **8**, 1–10.
- 55 C. T. Chudley and R. J. Elliott, *Proc. Phys. Soc., London*, 1961, **77**, 353–361.
- 56 P. L. Hall and D. Ross, *Mol. Phys.*, 1981, **42**, 673–682.
- 57 M. K. Gupta, R. Mittal, S. K. Mishra, P. Goel, B. Singh, S. Rols and S. L. Chaplot, *J. Phys.: Condens. Matter*, 2020, **32**, 505402.
- 58 K. Skold and D. L. Price, *Neutron scattering*, Academic Press, Orlando, 1986.
- 59 J. M. Carpenter and D. L. Price, *Phys. Rev. Lett.*, 1985, **54**, 441–443.
- 60 S. Rols, H. Jobic and H. Schober, *C. R. Phys.*, 2007, **8**, 777–788.
- 61 K. Burke, J. Perdew and M. Ernzerhof, *Phys. Rev. Lett.*, 1997, **78**, 1396.
- 62 J. P. Perdew, K. Burke and M. Ernzerhof, *Phys. Rev. Lett.*, 1996, **77**, 3865.
- 63 H. J. Monkhorst and J. D. Pack, *Phys. Rev. B: Solid State*, 1976, **13**, 5188–5192.
- 64 A. Togo and I. Tanaka, *Scr. Mater.*, 2015, **108**, 1–5.
- 65 B. Singh, M. K. Gupta, R. Mittal and S. L. Chaplot, *J. Mater. Chem. A*, 2018, **6**, 5052–5064.
- 66 S. Nosé, *J. Chem. Phys.*, 1984, **81**, 511–519.
- 67 M. P. Allen and D. J. Tildesley, *Computer simulation of liquids*, Oxford university press, 2017.
- 68 A. K. Sagotra, D. Chu and C. Cazorla, *Phys. Rev. Mater.*, 2019, **3**, 035405.
- 69 R. Mittal and S. L. Chaplot, *Phys. Rev. B: Condens. Matter Mater. Phys.*, 1999, **60**, 7234–7237.
- 70 R. Mittal, S. L. Chaplot, H. Schober and T. A. Mary, *Phys. Rev. Lett.*, 2001, **86**, 4692–4695.
- 71 J. Sugiyama, K. Mukai, Y. Ikedo, H. Nozaki, M. Månsson and I. Watanabe, *Phys. Rev. Lett.*, 2009, **103**, 147601.
- 72 T. Shibata, Y. Fukuzumi, W. Kobayashi and Y. Moritomo, *Sci. Rep.*, 2015, **5**, 1–4.
- 73 E. Rucavado, F. Landucci, M. Döbeli, Q. Jeangros, M. Boccard, A. Hessler-Wyser, C. Ballif and M. Morales-Masis, *Phys. Rev. Mater.*, 2019, **3**, 084608.
- 74 M. K. Gupta, R. Mittal, S. Kumar, B. Singh, N. H. Delaire, R. Shukla, S. N. Achary, A. I. Kolesnikov, A. K. Tyagi and S. L. J. a. p. a. Chaplot, 2021.
- 75 G. Henkelman and H. Jónsson, *J. Chem. Phys.*, 2000, **113**, 9978–9985.
- 76 M. Guidon, F. Schiffmann, J. Hutter and J. VandeVondele, *J. Chem. Phys.*, 2008, **128**, 214104.
- 77 S. S. R. K. C. Yamijala, Z. A. Ali and B. M. Wong, *J. Phys. Chem. C*, 2019, **123**, 25113–25120.
- 78 J. Wang, J. Ding, O. Delaire and G. Arya, *ACS Appl. Energy Mater.*, 2021, **4**, 7157–7167.
- 79 S. Adams, *Acta Crystallogr., Sect. B: Struct. Sci.*, 2001, **57**, 278–287.
- 80 H. Chen, L. L. Wong and S. Adams, *Acta Crystallogr., Sect. B: Struct. Sci., Cryst. Eng. Mater.*, 2019, **75**, 18–33.
- 81 D. Urushihara, S. Kawaguchi, R. Harada, T. Asaka and K. Fukuda, *Mater. Lett.*, 2020, **277**, 128373.
- 82 J. Rodríguez-Carvajal, *Phys. B*, 1993, **192**, 55–69.
- 83 B. Fultz, T. Kelley, J. Lin, J. Lee, O. Delaire, M. Kresch, M. McKerns and M. Aivazis, *Experimental inelastic neutron scattering: Introduction to DANSE*, 2009.

